

Moving Contact Lines: Scales, Regimes and Transitions

JACCO H. SNOEIJER

Physics of Fluids Group, Faculty of Science and Technology,

Mesa+ Institute, University of Twente, 7500AE Enschede, The Netherlands

BRUNO ANDREOTTI

Laboratoire de Physique et Mécanique des Milieux Hétérogènes,

(PMMH UMR 7636 ESPCI - CNRS - Univ. Paris Diderot - Univ. P. M. Curie.)

10 rue Vauquelin, 75005 Paris, France.

Key Words Wetting, spreading, wetting transitions, lubrication, contact angle,
interface dynamics

Abstract The speed at which liquid can move over a solid surface is strongly limited when a three-phase contact line is present, separating wet from dry regions. When enforcing large contact line speeds this leads to entrainment of drops, films or air bubbles. In this review we discuss experimental and theoretical progress revealing the physical mechanisms behind these dynamical wetting transitions. In this context we discuss microscopic processes that have been proposed to resolve the moving contact line paradox, and identify various dynamical regimes of contact line motion.

CONTENTS

Introduction 3

Static versus dynamic contact lines 4

Basic concepts 4

The singular flow geometry near a contact line 5

Coupling of molecular to macroscopic scales 7

Macroscopic scales: apparent contact angle 7

Mesosopic scales: hydrodynamic regime 9

Matching 10

Dynamical wetting transitions 12

Entrainment of liquid films 12

V-shaped contact lines 13

Dewetting holes 15

Entrainment of air 17

Molecular processes 18

Slip length, disjoining pressure, diffuse interface models 19

Thermally activated processes 23

Dynamical wetting regimes 27

Hydrodynamic versus thermally activated regime 27

Inertial effects 28

Future issues 29

Key Terms 40

Sidebar, to be placed after Section 2.2: Evaporation 41

1 Introduction

Those who have already looked at the slow motion of droplets on the window of a fast train are aware that a macroscopic flow can be strongly affected by interactions at molecular scales. Namely, the droplets are governed by the wetting dynamics of the contact line, which is the line that separates “wet” regions from “dry” regions. This contact line motion is ultimately determined by the physico-chemical interactions with the substrate, as is exemplified in Fig. 1: the hydrophobicity of an impacting sphere, which can be altered by a coating of a few nanometers thick, controls the outcome of a macroscopic splash. Understanding and modeling of such wetting dynamics have been, in the last decades, the subject of intense activity at the forefront of fluid mechanics, chemistry and engineering. In recent years, the main progress has been on understanding the multi-scale nature of the flow and how this gives rise to dynamical transitions such as shown for the splash in Fig. 1. In addition, the increasing control over surface properties has led to a wealth of new phenomena, such as superhydrophobicity, while the complexity of liquids and their solutes can give rise to intricate patterning and self-assembly as shown in Fig. 2. In many cases, the research is motivated by numerous applications encountered in industrial processes and ranging from oil recovery to imbibition of powders, from microfluidics and inkjet printing to the deposition of pesticides on plant leaves.

In this review, we will focus on a single fundamental problem of wetting dynamics: the motion of a contact line over a smooth substrate. We will not touch upon other contemporary issues like superhydrophobic substrates, Marangoni driven flows, evaporation, electrowetting, which involve dynamic contact lines in relatively complex situations – for reviews see Bonn et al. (2009), Craster & Matar

(2009), Mugele & Baret (2005), Roach et al. (2008). Rather, we focus on the nature of *dynamical wetting transitions* that occur at large driving velocities: these transitions lead to entrainment of films, drops or air bubbles (Fig. 1). In many applications, such as coating and immersion lithography, these entrainment phenomena are crucial limiting factors for industrial processes. From a fundamental perspective, the dynamical wetting transition forms an ideal testing ground for the various models of contact line motion: it provides more complete information than e.g. the dynamic contact angle, which is classically used to compare different models.

The paper first introduces basic concepts of static and dynamic contact lines in Section 2, while Section 3 highlights the multi-scale nature of the moving contact line problem. We then extensively review experimental and theoretical work on dynamical wetting transitions in Section 4, and discuss the influence of molecular process on contact line motion in Section 5. The paper closes with a summary of different regimes of contact line motion and lists some future issues in Section 6.

2 Static versus dynamic contact lines

2.1 Basic concepts

From a thermodynamic point of view, the molecular forces give rise to a surface tension that is defined as Gibbs free energy per surface area of an interface separating two phases (de Gennes et al. 2002, Rowlinson & Widom 1982). Equivalently, from a mechanical point of view, surface tension is the resultant force per unit length due to a normal stress anisotropy in the vicinity of the interface (Kirkwood & Buff 1949). For curved interfaces this gives rise to a pressure jump, also called Laplace pressure. The equilibrium shape of a meniscus climbing a wall,

or of puddle of liquid on a surface, results from the balance between this surface tension γ , and gravity g . The balance is governed by a characteristic length-scale given by the capillary length $\ell_\gamma = \sqrt{\gamma/\rho g}$, where ρ is the liquid density, which is typically a millimeter.

At the three-phase contact line, the wettability of the surface determines the equilibrium contact angle θ_e of the liquid on the solid. Minimization of Gibbs free energy shows that θ_e is determined by a balance of solid-vapor, solid-liquid, and liquid-vapor surface tensions:

$$\cos \theta_e = \frac{\gamma_{SV} - \gamma_{SL}}{\gamma}, \quad (1)$$

which is known as Young's law (de Gennes et al. 2002). Throughout, we use γ for the surface tension of a liquid-vapor (or liquid-gas) interface. In practice, even the cleanest surfaces are not perfectly homogeneous, and exhibit chemical or geometrical heterogeneities (Bonn et al. 2009). This unavoidably leads to contact angle hysteresis, where static contact angles can be achieved in a range $\theta_r < \theta < \theta_a$. Here $\theta_{a,r}$ are called advancing and receding contact angles respectively. This emphasizes that the contact angle is selected at a molecular scale (Snoeijer & Andreotti 2008), and the contact angle therefore acts as a boundary condition for the macroscopic interface.

2.2 The singular flow geometry near a contact line

The situation is completely different when the contact line moves with respect to the substrate, for which the system is no longer at equilibrium. Even for an infinitesimal velocity U , the six decades separating the molecular size (nanometer scale) from the capillary length (millimeter scale) are the locus of a force absent from the static problem: viscosity. The hydrodynamics is in essence described by

a corner flow (Huh & Scriven 1971), which has no intrinsic length scale (Fig. 3). A few general conclusions can be drawn from this. First, the lack of intrinsic length scale of the flow means that one can only define a *local* Reynolds number, based on the distance to the contact line r . As this distance can become arbitrarily small, the Reynolds number is typically very small and inertia can often be neglected. Second, the viscous stress near the contact line scales as $\sim \eta U/r$, where η denotes the dynamical viscosity of the liquid. Hence, the shear stress diverges upon approaching $r = 0$. It is instructive to rephrase this in terms of the rate of energy dissipation \dot{E} (per unit contact line), which in between a distance r and $r + dr$ scales as (Bonn et al. 2009, de Gennes 1985)

$$d\dot{E} \sim \eta U^2 \frac{dr}{r} \sim \eta U^2 (d \ln r). \quad (2)$$

This implies that the total dissipation is not integrable at $r = 0$ nor at ∞ , and one requires a cut-off at both small scales and large scales. Typically, these cut-offs appear at molecular scale ($\sim 10^{-9}\text{m}$), and at the scale of the capillary length ℓ_γ ($\sim 10^{-3}\text{m}$). Each of the decades in between the microscopic scale and the macroscopic scale contributes a comparable amount to the viscous dissipation, revealing the *multi-scale* character of wetting flows.

These features of moving contact lines were first appreciated by Huh & Scriven (1971), who analytically solved the flow in a perfect wedge using similarity solutions. The viscosity-dominated flow is described by Stokes equations, which in two dimensions can be reduced to the biharmonic equation $\nabla^4 \psi = 0$. Here, $\psi(r, \phi)$ is the streamfunction expressed in polar coordinates (r, ϕ) . Using a no-slip boundary condition at the wall, $u_r = -U$, one derives the similarity solution for flow in a perfect corner $\psi(r, \phi) = Ur (A \cos \phi + B \sin \phi + C \phi \cos \phi + D \phi \sin \phi)$. The coefficients are determined by the four boundary conditions: the solid is

impermeable and allows no-slip, while the free surface is impermeable and has no-(shear)stress. The corresponding streamlines are sketched in Fig. 3, for one-phase and two-phase flows. The exact solutions by Huh & Scriven also reveal that there is a viscosity-induced pressure on the free surface. This pressure must be balanced by the capillary pressure and hence requires a curvature of the interface. The dimensionless number that describes this visco-capillary balance is the capillary number,

$$\text{Ca} = \frac{U\eta}{\gamma}, \quad (3)$$

which is the key parameter for moving contact lines.

3 Coupling of molecular to macroscopic scales

The interplay between the different length scales is illustrated using the paradigmatic example of dip-coating, which has obvious importance in coating applications. As sketched in Fig. 3, a partially wetting solid substrate is plunged into a liquid reservoir at a velocity U . The successive zooms near the contact line illustrate the physics at different scales. On the macroscopic scale of the capillary length ℓ_γ , the shape of the meniscus is governed by the balance of gravity and surface tension; at smaller scales one encounters a visco-capillary regime, characterized by the capillary number Ca . This section addresses the physics of these regimes and how they are coupled. The ultimate zoom in Fig. 3 is on the molecular scale, which will be treated separately in Sec. 5.

3.1 Macroscopic scales: apparent contact angle

When plunging the plate at moderate velocities, the meniscus attains a steady shape in the frame of the reservoir. Figure 4a shows experimental measurements

of the meniscus shape by Rame & Garoff (1996). The lower of the datasets is the shape at $Ca = 0$, which is accurately fitted by the analytical solution for an equilibrium profile (solid line). The upper dataset is the dynamical meniscus shape at $Ca = 0.1$. Here, the variation of the angle θ is non-monotonic: close to the contact line it increases with x , while it decreases again to connect to the bath at 90° . Again, the large scale solution can be accurately fitted to by the formula for a static meniscus solution. On smaller scales, one observes the onset of the viscosity-dominated hydrodynamic regime (Kavehpour et al. 2003, Rame & Garoff 1996).

Extrapolating the static outer solution (dotted line) towards the contact line leads to an *apparent* macroscopic contact angle, θ_{ap} , which in this case is approximately 120° . A simple way to extract θ_{ap} from an experiment is to measure the elevation of the contact line over the bath, z , using the static meniscus solution (Landau & Lifshitz 1984)

$$z = \ell_\gamma \sqrt{2(1 - \sin \theta_{ap})}. \quad (4)$$

Clearly, the apparent contact angle of a meniscus will depend on Ca , since it determines how far the system is pushed from equilibrium. For advancing contact lines $\theta_{ap} > \theta_e$ (as in Fig. 4a), while $\theta_{ap} < \theta_e$ in the receding case. In many flow situations, the apparent contact angle completely describes the dynamics. Examples are drop spreading (Hocking 1983), drops sliding down a window at low velocities (Ben Amar et al. 2003, Rio et al. 2005), or the relaxation of contact line perturbations (Golestanian & Raphaël 2001, Nikolayev & Beysens 2003, Snoeijer et al. 2007b).

3.2 Mesoscopic scales: hydrodynamic regime

3.2.1 THE VISCO-CAPILLARY BALANCE. We now turn to the hydrodynamic regime, emerging at distances below ℓ_γ , where the meniscus shape is influenced by viscous effects. This is most easily captured using the *lubrication approximation*, for which the angles are assumed small (Oron et al. 1997). The Stokes flow then reduces to the a third order differential equation for the interface profile $h(x)$, as defined in Fig. 3c,

$$\frac{d^3 h}{dx^3} = -\frac{\sigma \text{Ca}}{h^2}, \quad (5)$$

and expresses the balance between the capillary and the viscous stress. Here $\sigma = +1$ for advancing contact lines, $\sigma = -1$ for receding contact lines. With this convention Ca is considered positive for both advancing and receding cases.

3.2.2 THE VOINOV SOLUTION. Remarkably, the highly nonlinear Equation 5 has an exact solution (Duffy & Wilson 1997). In some specific asymptotic limits, the exact solution reduces to the form proposed by Voinov (1976),

$$h'(x) \approx \theta(x) \simeq [9\text{Ca} \ln(x/c)]^{1/3}. \quad (6)$$

This relation reveals the “viscous bending” of the interface: the contact angle varies logarithmically with the distance to the contact line. This asymptotic solution by Voinov is valid up to large distances $x \rightarrow \infty$ for advancing contact lines ($\sigma = 1$ in Equation 5), but not for receding contact lines ($\sigma = -1$). The solution has the convenient property that the macroscopic curvature $h''(\infty) = 0$, which can thus be imposed as a macroscopic matching condition for advancing contact lines. For receding contact lines the matching to macroscopic scales is more intricate (Eggers 2004, 2005).

Equation 6 can be generalized to flows with large contact angles, i.e. be-

yond the assumptions of the lubrication approximation (Cox 1986, Snoeijer 2006, Voinov 1976), by a perturbation expansion around the Huh & Scriven solutions. Surprisingly, the generalized result for $\theta(x)$ is almost identical to Equation 6, to within a few percent, up to angles as large as 150° . This means that Equation 6 is applicable to the experimental data for $\theta(x)$ shown in Fig. 4. Indeed, the Voinov solution very accurately describes the onset of the viscous regime, and bridges the gap between molecular scales and macroscopic scales.

3.3 Matching

The matching of the equilibrium solution to the mesoscopic/hydrodynamic solution provides the relation between θ_{ap} and Ca (Cox 1986, Hocking 1983, Voinov 1976). In cases where Equation 6 represents the correct asymptotics, the matching reduces to the ‘‘Cox-Voinov’’ law

$$\theta_{ap}^3 = \theta_e^3 + 9\sigma\text{Ca} \ln\left(\frac{\alpha\ell_o}{\ell_i}\right). \quad (7)$$

Here, ℓ_o is an outer (macroscopic) length (i.e. the capillary length or the size of a spreading drop), while ℓ_i is an inner (microscopic) length that represents the molecular processes that regularize the viscous singularity (which relates to c in Equation 6). The numerical constant α is a non-universal number that depends on details of the microscopic and macroscopic boundary conditions.

We emphasize that Equations 6 and 7 correspond to a particular solution of the hydrodynamic problem, and hence these are not universally applicable. A prime example that is not described by the Cox-Voinov relation is dip-coating with a reversed plate velocity, i.e. where the plate is *withdrawn* from the bath (Eggers 2004, 2005). In this case Equation 5 does not admit any solutions with $h''(\infty) = 0$ and the matching requires the full analytical solution by Duffy & Wilson (1997).

Figure 4b reveals the bifurcation diagram for steady-state solutions for plate withdrawal (Delon et al. 2008, Snoeijer et al. 2007b). The menisci are represented by the meniscus rise z , related to θ_{ap} according to Equation 4, for various plate velocities Ca . The maximum possible plate velocity, or critical capillary number Ca_c , is achieved at $z_c \approx \ell_\gamma \sqrt{2}$. This means that at the maximum speed $\theta_{ap} \approx 0$ (Chan et al. 2011, Maleki et al. 2007, Sedev & Petrov 1991, Snoeijer et al. 2007b), consistent with the conjecture by Deryaguin & Levi (1964) and with the matched asymptotic expansion by Eggers (2004). Interestingly, the steady-state solutions continue beyond this critical meniscus rise, onto a higher branch of meniscus solutions. It is impossible to attribute an apparent contact angle to these meniscus shapes based on Equation 4 (Chan et al. 2012).

Figure 4b illustrates that the menisci for plate withdrawal are governed by a nontrivial bifurcation scenario, which is predicted by hydrodynamics, but which reaches beyond a simple picture based on an apparent contact angle. How quantitative is the hydrodynamic prediction, e.g. for the critical speed Ca_c ? The lubrication model leading to the solid line in Fig. 4b accounts only for the viscous dissipation in between the microscopic scale, here characterized by a slip length of two molecular sizes, and the capillary length. The *microscopic contact angle* was assumed equal to the receding equilibrium angle θ_r . We emphasize that the hydrodynamic prediction is quite sensitive to the microscopic contact angle: the few degrees of uncertainty related to contact angle hysteresis induce variations of the critical Ca_c by as much as 20%. The precise value of the slip length only weakly (logarithmically) affects the results. We return to this important point in Sec. 5 where molecular process are reviewed in detail. However, as any other source of dissipation would add up to viscous dissipation, this quantitative

agreement with experiments suggests that most of the dissipation takes place in the hydrodynamic scales (roughly from 10 nm to 1 mm).

4 Dynamical wetting transitions

An interesting situation arises when a liquid is forced to flow over a surface that it does not spontaneously wet in thermodynamic equilibrium. In such partial wetting conditions, it is energetically favorable for the liquid to stick together as much as possible and to leave most of the surface dry. However, an external driving of the flow can push the system sufficiently far from equilibrium such that it undergoes a *dynamical wetting transition*. In practical terms, this means that the contact line motion cannot exceed a maximum speed: enforcing larger velocities leads e.g. to deposition of liquid films, break-up of liquid drops or entrainment air bubbles. In this section we summarize recent experimental and theoretical progress on the nature of these dynamical wetting transitions.

4.1 Entrainment of liquid films

One of the simplest ways to deposit a thin film of liquid is by withdrawing a solid from a reservoir (Fig. 4). The geometry is identical to the dip-coating in Fig. 3, but now with a reversed velocity of the substrate such that the contact line is receding. Under complete wetting conditions, this dip-coating gives a uniform film of thickness that is controlled by the speed of withdrawal. This goes back to pioneering work by Landau & Levich (1942) and Deryaguin (1943), who demonstrated that the thickness $h_{LLD} \sim \ell_\gamma Ca^{2/3}$.

The situation is much more complex when the liquid is partially wetting the solid. Figure 4b showed that the contact line can rise to a steady position without

leaving a film when the speed of withdrawal is sufficiently small (Snoeijs et al. 2007b). Above a critical Ca_c , however, steady-state solutions cease to exist and a dynamical wetting transition occurs (Blake & Ruschak 1979, Eggers 2004, Quéré 1991, Sedev & Petrov 1991, Snoeijs et al. 2006). The physics of this dynamical wetting transition is that above the critical speed, the capillary forces can no longer compete with the large viscous forces that develop inside the flow (de Gennes 1985).

Above the critical speed, one observes the dynamical evolution of a liquid film that is very different from the smooth Landau-Levich film (Fig. 4c). The dynamical film solution splits into two parts, due to a mismatch of microscopic and macroscopic boundary conditions (Snoeijs et al. 2006). Immediately behind the contact line there is a thick film of thickness h_f , which is determined by the microscopic boundary conditions imposed at the contact line. At the side of the reservoir one observes the Landau-Levich-Derjaguin film. The two solutions are connected by a shock that travels upwards with respect to the reservoir, at a velocity described accurately by lubrication theory (Snoeijs et al. 2006). In terms of the capillary number, the thickness in front of the shock $h_f \sim \ell_\gamma Ca^{1/2}$, which at small Ca is indeed thicker than $h_{LLD} \sim \ell_\gamma Ca^{2/3}$.

4.2 V-shaped contact lines

4.2.1 REDUCING THE CONTACT LINE NORMAL SPEED. Stability analysis has shown that an infinitely extended, straight contact line is linearly stable for all capillary numbers, all the way up to the critical point (Golestanian & Raphaël 2001, Snoeijs et al. 2007b). Experimentally, however, the finite lateral extension of the contact line has major practical consequences. This can already be seen

from the image in Fig. 4c: no entrainment occurs at the sharp edge of the wafer, inducing a sharp kink in the contact line higher up the solid. Indeed, such *corners*, or *V-shapes* are a generic feature of moving contact lines near the transition. Figure 5 represents a broad collection of contact lines that spontaneously develop a V-shape (Blake & Ruschak 1979, Delon et al. 2008, Duez et al. 2007, Le Grand et al. 2005, Peters et al. 2009, Podgorski et al. 2001, Winkels et al. 2011). In all experiments, the corners start to emit little droplets (receding contact lines) or bubbles (advancing contact lines) when moving at even higher speeds.

The formation of a corner is a very elegant way to “delay” the dynamical wetting transition. The physical mechanism, first described by Blake & Ruschak (1979), is that the inclination of the contact line reduces the normal velocity, $U_{\perp} \sim U \sin \phi$. Here, ϕ is the top-view angle of the corner. As the local fluid velocity near the contact line is equal to U_{\perp} (Rio et al. 2005), the effective driving is reduced by a factor $\sin \phi$. In analogy to the “Mach cone” for supersonic flows, it was proposed that $\sin \phi \sim U_c/U$, in order to maintain a normal velocity below the critical speed U_c (Blake & Ruschak 1979, Podgorski et al. 2001).

4.2.2 THE CASE OF SLIDING DROPS. The dewetting corners appearing at the rear of sliding drops can be understood from a model that considers the tip of the corner to be infinitely sharp. By assuming a perfect conical geometry of the interface, Limat & Stone (2004) identified a similarity solution that describing the three-dimensional shape of the interface. Defining the coordinates (x, y) as in Fig. 5d, these solutions are of the form $h(x, y) = x\Omega\text{Ca}^{1/3}\mathcal{H}(y/x)$, where Ω is the side-view angle and \mathcal{H} is the cross-sectional similarity profile of the cone. The cone-solution has a vanishing interface curvature along the central axis in the direction of the flow, i.e. $\partial^2 h/\partial x^2 = 0$. This is fundamentally different from

straight contact lines, since for the corners the side-view angle $\partial h/\partial x = \Omega$ no longer varies with x . Instead, the driving capillary forces inside a corner originate from the *transverse curvature*, $\partial^2 h/\partial y^2 \sim \text{Ca}/x$. This three-dimensional feature is not captured by the Mach-cone argument, and is crucial for explaining the pearling transition (Snoeijer et al. 2007a).

The fine structure of the corner tip can be characterized by the curvature $1/R$ of the contact line. Figure 5 shows the tip curvature for different speeds before the pearling transition (Peters et al. 2009). While at small velocities $1/R$ is approximately constant, the tip curvature increases dramatically near the transition. This can be understood quantitatively from a variation of the Cox-Voinov relation, Equation 7. At a small distance from the tip, much smaller than R , the contact line is effectively straight. In this regime one expects the usual contact line dynamics characterized by an inner microscopic scale ℓ_i . The behavior changes at a distances of order R , where the geometry becomes truly three-dimensional and the transverse curvature is the dominant capillary driving. Interpreting Equation 7 as an equation for R , one obtains

$$R = \alpha^{-1} \ell_i \exp\left(\frac{\theta_e^3 - \theta_{ap}^3}{9\text{Ca}}\right) \approx \alpha^{-1} \ell_i \exp\left(\frac{\theta_e^3}{9\text{Ca}}\right). \quad (8)$$

This relation is represented as the solid line in Fig. 5. It accurately describes the experimental data, upon fitting a microscopic length $\alpha^{-1}\ell_i = 7\text{nm}$.

4.3 Dewetting holes

Another class of dewetting transitions is encountered after a partially wetting surface is covered by a macroscopic liquid film. Thermodynamically, such a film is metastable since the surface free energy can be reduced by collecting the film

into liquid drops. There are two mechanisms leading to dewetting. The first is encountered when the thickness falls within the range of microscopic interactions (typically 2 – 10 nm). This induces a so-called spinodal instability that is characterized by a well-defined wavelength (Reiter 1992, Saulnier et al. 2002, Seemann et al. 2001, Thiele 2003). A second mechanism is induced by large amplitude perturbations: once a small hole is nucleated inside the film and a contact line appears, the hole will rapidly grow and dewet the surface (Brochard-Wyart et al. 1987, de Gennes et al. 2002, Redon et al. 1991). Here we consider the second mechanism, which involves the dynamics of a moving contact line. Figure 6 shows a snapshot of a hole for the dewetting of an air film (Fig. 6a) and for a liquid film (Fig. 6b). As the contact line bordering the film retracts over the solid, the liquid or air inside the film is collected into a rim, which grows slowly in time. It is found experimentally that the speed of retraction of a viscous film is constant (Redon et al. 1991).

The problem consists essentially of a receding front at the contact line forming the front of the rim, coupled to an advancing front forming the back of the rim. The dewetting speed is determined by equating θ_{ap} for the advancing front to θ_{ap} of the receding front (de Gennes et al. 2002). This viewpoint was confirmed recently by matched asymptotic expansion of the lubrication equations (Flitton & King 2004, Snoeijer & Eggers 2010). The solid line in Fig. 6d represents an exact solution of Equation 5, which is matched to the advancing front denoted by the dashed line. As a result, it was found that the appropriate law for $\theta_{ap}(Ca)$ was not the classical result by de Gennes (1986), as was previously assumed (de Gennes et al. 2002), but the Cox-Voinov relation. The advancing front is described by Equation 7, with $\theta_e = 0$, and involves the rim-width w and film thickness h_f as

relevant length scales. The receding contact line ($\sigma = -1$) involves a ratio w/λ , where ℓ_s is the slip length. Equation the advancing and receding θ_{ap} , the velocity was found Snoeijer & Eggers (2010)

$$\text{Ca} = \frac{\theta_e^3}{9} \left[\ln \left(\frac{4a\theta_e \text{Ca}^{1/3}}{3e} \frac{w^2}{\ell_s h_f} \right) \right]^{-1}, \quad (9)$$

where a is the numerical constant $a = 1.094 \dots$. Figure 6c replots the dewetting speeds for different liquids and wettabilities obtained by Redon et al. (1991). Here, the factor L represents the logarithmic factor in Equation 9, where the slip length ℓ_s was estimated as $2\sqrt{N}a$, where the N is the number of monomers and a the monomer size (cf. Sec. 5.1).

4.4 Entrainment of air

The dynamical wetting transition for advancing contact lines results into the entrainment of air. The splash in Fig. 1 arises when the contact line cannot advance sufficiently fast over the solid to close the cavity in the wake of the sphere (Duez et al. 2007). For very hydrophobic surfaces, the splashing threshold scales as $\text{Ca} \sim (\pi - \theta_e)^3$ (Fig. 1a). This is strongly reminiscent of the θ_e^3 dependence characteristic for receding contact lines (see e.g. Equation 9). This suggests that the critical speed is governed by the gas-phase, which consists of a wedge of angle $\pi - \theta_e$ and which is receding over the solid (Fig. 3b). A similar dependency on θ_e was found for drop emission by liquid filaments and in simulations (Do-Quang & Amberg 2009, Ledesma-Aguilar et al. 2011).

The mutual influence of the liquid and gas phases on air entrainment was mostly investigated in the context of dip-coating (Benkreira & Ikin 2010, Benkreira & Khan 2008, Blake & Ruschak 1979, Burley & Kennedy 1978, Marchand et al. 2012, Simpkins & Kuck 2000). These experiments typically vary the dynamical

viscosity of the liquid phase η : the critical speed decreases for more viscous liquids, suggesting that dissipation in the liquid is important. However, the dependency is much less than the expected $\sim 1/\eta$. Marchand et al. (2012) showed that this can be attributed to the gas viscosity: the dissipation in the air becomes significant due to the confinement of the wedge of air (Fig. 3b). Another striking effect is that the critical speed increases when reducing the air pressure to about 1-10% atmosphere. Since such a pressure change does not affect the gas viscosity, this effect must be due to inertia in the gas or due to the increase of the mean free path. The latter would imply a larger slip length, which reduces the dissipation in the gas and leads to a larger critical speed (Marchand et al. 2012). Similar effects of the gas phase were observed in drop splashing (De Ruiter et al. 2012, Mandre et al. 2009, Tsai et al. 2010, Xu et al. 2005). A definitive description of the role of the air in dip-coating and in splashing is still lacking.

5 Molecular processes

An important conclusion reached in nano-fluidics is that the Navier-Stokes equations remain valid for liquid layers down to nanometer scale for simple fluids like water, under normal conditions (Bocquet & Charlaix 2010). This means that in between ~ 10 nm from the contact line up to macroscopic scales, the shape of a moving interface can be described by continuum hydrodynamics. In this section we review different processes that becomes relevant at the scale where hydrodynamics breaks down. We anticipate that all descriptions require two physical quantities: a length scale to point out at what scale microscopic processes start to play a role, and an energy scale that expresses the strength of the interaction with the solid (i.e. the wettability). The section first concentrates on mechanisms that

are commonly used in combination with continuum hydrodynamics, for example in the context of numerical simulations involving moving contact lines (Sec. 5.1). We then turn to thermally activated processes (Sec. 5.2), where we point out the similarities and differences with the hydrodynamic theory.

5.1 Slip length, disjoining pressure, diffuse interface models

5.1.1 SLIP LENGTH. It is by now well-established that motion of the first few molecular layers above a solid substrate can be described by the Navier slip boundary condition :

$$u_{z=0} = \ell_s \frac{\partial u}{\partial z}, \quad (10)$$

where ℓ_s is called the slip length and $z = 0$ denotes the position of the wall. For gases, the existence of velocity slip in a gas was first predicted by Maxwell (1878) who argued that the slip length must be proportional to the mean free path ℓ_{mfp} . This proportionality $\ell_s \sim \ell_{\text{mfp}}$ was demonstrated experimentally (Andrew & Harris 1995), numerically (Morris et al. 1992) and analytically (Bocquet 1993), with a proportionality constant 2.4 in experiments. For liquids, a fully microscopic prediction for the slip length was derived from statistical physical theory of liquids (Huang et al. 2008):

$$\ell_s \sim \frac{\eta Da k_B T}{(\gamma a^2 (1 + \cos \theta_e))^2} a. \quad (11)$$

This expression contains the molecular size a , the self-diffusion coefficient D , and a wettability factor $\gamma(1 + \cos \theta_e)$ that arises from the tangential forces on the liquid near the wall. Indeed, the dependence $(1 + \cos \theta_e)^{-2}$ is approximately verified in experiments and in numerical simulations (Bocquet & Charlaix 2010, Huang et al. 2008). Moreover, for simple liquids, the Stokes-Einstein relation is approximately valid and leads to $\eta Da \sim k_B T$. As a consequence, the slip length

ℓ_s is not expected to depend on the liquid viscosity for simple liquids. Polymer solutions typically exhibit much larger slip lengths on the order of the molecule size $2\sqrt{N}a$, where the N is the number of monomers and a the monomer size.

5.1.2 SLIP AND MOVING CONTACT LINES. For moving contact lines, the Navier slip condition leads to a regularization of the viscous stress divergence that was discussed in Sec. 2.2: in the lubrication approximation, the viscous stress applied to the solid by a flowing film of thickness h is $3\eta U/(h + 3\ell_s)$ and the rate of dissipation per unit contact line becomes

$$\dot{E} = \frac{1}{2}\eta U^2 \int \frac{3h}{(h + 3\ell_s)^2} dx. \quad (12)$$

This is now a convergent integral as the layer thickness $h \rightarrow 0$.

The Navier slip boundary condition is a popular treatment to remove the moving contact line singularity: it is well-established experimentally and theoretically, and it is easily incorporated into a continuum description. However, we wish to point out a few limitations of the method. The main problem is that the slip condition introduces only a length scale, but not an energy scale that expresses the interaction with the solid wall. In practice this means that the hydrodynamic equations still lack a boundary condition for the microscopic contact angle, which is necessary to close the problem. Second, the introduction of slip regularizes the divergence of shear stress and energy dissipation, but it still leads to a logarithmically divergent pressure $p \sim \eta U/\ell_s \ln(h/\ell_s)$ (Buckingham et al. 2003).

5.1.3 DISJOINING PRESSURE. This interaction with the solid substrate can be introduced using an effective interface potential (de Feijter 1988). A common approximation is to write the interfacial free energy functional (per unit contact

line):

$$\mathcal{F}[h(x)] = \int dx \left[\gamma \left(\sqrt{1 + h'^2} - 1 \right) + \omega(h) \right]. \quad (13)$$

The first term represents the capillary energy of the liquid-vapor interface, while $\omega(h)$ is an effective potential due to the finite thickness of the layer h . Taking the functional derivative of Equation 13, one obtains the pressure discontinuity across the interface, $\delta\mathcal{F}/\delta h(x) = -\gamma\kappa + \Pi(h)$. The first term is the Laplace pressure due to interface curvature κ . The second is the disjoining pressure (or internal energy per unit volume), defined as $\Pi(h) = d\omega/dh$. Descriptions beyond Equation 13 leads to more complex nonlocal equations for the capillary pressure (Getta & Dietrich 1998, Merchant & Keller 1992, Snoeijer & Andreotti 2008).

The most common numerical treatment involving a disjoining pressure is to introduce a functional form for $\omega(h)$ that exhibits a minimum $\omega'(h = h^*) = 0$. Then, the liquid interface tends to a precursor film of thickness h^* , for which the disjoining pressure $\Pi(h^*) = 0$ (Pismen 2001, Pismen & Pomeau 2000, Schwartz et al. 2005, Thiele et al. 2002). This method has the convenient property that it leads to both a selection of the microscopic contact angle and to regularization of the viscous stress, even without explicitly using the Navier boundary condition. The introduction of such a disjoining pressure avoids the caveats of the slip model. From a physical perspective, the drawback is that precursor films are usually not encountered under partially wetting conditions. It is, however, possible to include a $\Pi(h)$ that does not lead to precursor films (Colinet & Rednikov 2011, de Gennes et al. 1990).

5.1.4 DIFFUSE INTERFACE MODELS. Up to now we have implicitly assumed that the liquid-vapor interface is characterized by a mathematically sharp profile $h(x)$. One should bear in mind that the interface has a finite width, typically a

few molecular sizes (Rowlinson & Widom 1982). This can be characterized by a variation in the (coarse grained) density field $\phi(\vec{r})$, which smoothly connects the high density liquid phase to the low density vapor phase. The jump in density occurs over a scale ζ , the interface width. From the perspective of continuum hydrodynamics, the capillary forces inside the diffuse interface are described by a force per unit volume $\sim \nabla\phi$, which has to be incorporated in the Navier-Stokes equation (Jacqmin 2000, Qian et al. 2004, 2006, Yue & Feng 2011).

The diffuse interface framework is very popular for numerical simulations, in particular when the flow geometry does not allow for a lubrication approximation. Even if the no-slip boundary condition is applied, the contact line can move through phase transition (for a liquid-vapor interface) or by diffusion (for two immiscible liquids). The characteristic length scale over which the phase transformation or diffusion occurs is determined by the diffusion length, ℓ_D , which is a priori independent from the interface width ζ (Qian et al. 2006, Ren & E 2007). If a Navier slip boundary condition is imposed, the effective slip observed on a macroscopic scale is determined by the larger of the two lengths ℓ_s or ℓ_D . In addition, generalizations of the Navier slip boundary conditions have been proposed to account for the stresses inside the diffuse interface (Carlson et al. 2009, Qian et al. 2006, Ren & E 2007). In the simplest version, slip velocity is dominated by the unbalanced Young stress, leading to a law for the *microscopic* contact angle:

$$\cos\theta - \cos\theta_e \sim \text{Ca} \frac{\zeta}{\ell_s} \quad (14)$$

Note that for typical fluids, the lengths ζ , ℓ_D and ℓ_s are expected to be of comparable magnitude.

5.2 Thermally activated processes

5.2.1 MOLECULAR KINETIC THEORY FOR CONTACT LINE MOTION. A rather different perspective on the dynamics of wetting is to consider that contact line motion is a thermally activated process (Blake 2006, Blake & De Coninck 2011, Blake & Haynes 1969, Seveno et al. 2009). The key idea of this Molecular Kinetic Theory (MKT), is that contact line moves by small “jumps” induced by thermal fluctuations. Indeed, thermal noise leads to a stochastic stress inside the liquid that can compete with viscous and capillary stresses. For example, the thermal length $\ell_T = \sqrt{k_B T / \gamma}$ is the scale below which thermal activation can dominate capillary forces, inducing a “roughening” of the surface (Flekkoy & Rothman 1996).

A full derivation of contact line hydrodynamics including thermal fluctuations has not yet been attempted. However, MKT provides a phenomenological description that treats contact line motion as a single mode of propagation, characterized by a length scale ξ , and by an energy barrier for the activated process E^* (Blake 2006). The activation length ξ is subnanometric and the energy barrier is of the order of the solid-liquid interaction, $E^* \sim \gamma^2 \xi^2 (1 + \cos \theta_e)$. Using the reaction rate theory for thermal activation (Hanggi et al. 1990), the frequency at which the barrier is crossed is $\nu = \nu_0 \exp\left(-\frac{E^*}{k_B T}\right)$, where ν_0 is the attempt frequency. For molecular motion, the attempt frequency is typically the thermal frequency $\nu_0 \sim k_B T / h \sim 10^{13}$ Hz, where h is Planck’s constant.

If the system is submitted to a driving force F , a quantity of energy $\pm F\xi/2$ is imparted to the particle in the form of work during an elementary contact line movement. The plus (minus) sign arises when the motion is in the direction of (opposite to) the direction of the force. As a consequence, the contact line

moves with an average velocity $U = \xi(\nu_+ - \nu_-)$, determined by the net frequency of forward and reverse jumps $\nu_{\pm} = \nu_0 \exp\left(\frac{-E^* \pm F\xi/2}{k_B T}\right)$. For a contact line with non-equilibrium angle θ , the unbalanced capillary force $F = \gamma\xi(\cos\theta_e - \cos\theta)$. This way, one obtains the central MKT result (Blake & Haynes 1969):

$$U = 2\nu_0\xi \exp\left(-\frac{E^*}{k_B T}\right) \sinh\left(\frac{\gamma\xi^2(\cos\theta_e - \cos\theta)}{2k_B T}\right). \quad (15)$$

This relation predicts the contact line speed as a function of the driving force $\cos\theta_e - \cos\theta$. We emphasize that θ must be interpreted as a truly *microscopic* contact angle, defined on a molecular scale ξ , which is fundamentally different from the apparent (macroscopic) contact angle θ_{ap} . In the hierarchy of scales in Fig. 3c, the angle θ applies to the zoom on molecular scales while θ_{ap} applies to the largest scale meniscus profile.

The arguments of the Boltzmann factors in Equation 15 scale with $\gamma\xi^2/k_B T = (\xi/\ell_T)^2$. In the original interpretation of MKT, this ratio of length scales is order unity. Hence, one can approximate $\sinh(x) \simeq x$, and one recovers a linear relation between speed and driving force (Seveno et al. 2009). In this interpretation, MKT does not represent any contact angle hysteresis: the limit of vanishing velocity gives the same value for θ_e , both for advancing contact lines ($U \downarrow 0$), as for receding contact lines ($U \uparrow 0$).

5.2.2 RELATION TO EYRING'S VISCOSITY. The MKT is based on the same phenomenological principles as Eyring's theory for the viscosity of liquids (Blake & De Coninck 2011). In a bulk liquid, ξ is interpreted as the size of a molecular rearrangement, induced by a shear stress τ . Taking $F = \tau\xi^2$, and following the steps of the preceding paragraph, one obtains Eyring's formula for the liquid

viscosity:

$$\eta = \frac{k_B T}{\nu_0 \xi^3} \exp\left(\frac{E_\eta}{k_B T}\right). \quad (16)$$

The activation energy E_η is due to liquid-liquid interactions, and can be estimated by the liquid-liquid adhesion energy $E_\eta \sim 2\gamma\xi^2$. This phenomenological description provides a realistic estimate for the viscosity of simple liquids (Monnery et al. 1995). Note that the polymeric liquids standardly used in labs to reach high viscosities (e.g. glycerol) cannot be described by Eyring’s viscosity model as they present a glassy dynamics.

Combining the Eyring viscosity with the linearized MKT, Equation 15 gives

$$U = \frac{\gamma}{\eta} \exp\left(\frac{E_\eta - E^*}{k_B T}\right) (\cos \theta_e - \cos \theta). \quad (17)$$

The energy $E_\eta - E^*$ appearing in the Boltzmann factor is typically on the order of $\gamma\xi^2(1 - \cos \theta_e)$, such that the Boltzmann factors are once more of order unity. As the viscosity now appears explicitly in Equation 17, the MKT can be interpreted in a hydrodynamic framework. On the scale of the first molecular layers, the balance of viscous stresses and capillary force would induce a “bending” of the surface by an amount $\cos \theta_e - \cos \theta \sim \text{Ca}$. This relation is of the same form as Equation 14, except that the ratio ζ/ℓ_s is replaced by a Boltzmann factor of order unity. From this perspective, the MKT theory should not be considered as an alternative to the hydrodynamical description, but as another slip model for the molecular scale boundary condition.

5.2.3 DISSIPATION INDUCED BY SURFACE HETEROGENEITIES. Substrates generically present heterogeneities of chemical or geometrical origin. These heterogeneities can be modeled as effective energy barriers, that have a characteristic width ξ and height E^* . Although not designed for that purpose, the MKT model

turns out to provide an effective description of contact line motion due to activated processes, in the presence of substrate heterogeneities (Prevost et al. 1999, Rolley & Guthmann 2007). Figure 7a shows the velocity of a moving contact line as a function of the apparent contact angle, in the vicinity to the threshold of depinning. Over a very small range of apparent contact angles (about two degrees), one observes an exponential increase of the velocity. This is consistent with the thermal activation model of Equation 15, provided that $\xi/\ell_T \gg 1$. A fit of the experimental data reveal an activation length-scale ξ of typically 10 nm, which is at least one order of magnitude larger than ℓ_T . Introducing the dimensionless number $H = E^*/\gamma\xi^2$, the MKT theory can be written as:

$$U \simeq 2\nu_0\xi \exp\left(-\frac{\xi^2}{\ell_T^2} [H + \cos\theta_e - \cos\theta]\right). \quad (18)$$

Bearing in mind that $(\xi/\ell_T)^2 \simeq 10^3$, this expression predicts a quasi-discontinuity of the microscopic contact angle across $\text{Ca} = 0$: the contact line velocity can only become significant when the energy barriers disappear, for $\cos\theta \simeq \cos\theta_e \pm H$. Therefore, H is naturally interpreted as the contact angle hysteresis: $H = \frac{1}{2}(\cos\theta_r - \cos\theta_a)$, where $\theta_{a,r}$ are the advancing and receding contact angles. Since the length scale of the activation is now much larger than ℓ_T , one can no longer interpret ν_0 as the thermal attempt frequency. Following Kramers' analysis (Hanggi et al. 1990, Kramers 1940), the attempt frequency ν_0 is given by the well oscillation frequency $\nu_0 \sim \sqrt{\gamma H/\rho\xi^3}$ in the underdamped regime and by the dissipative frequency $\nu_0 \sim H\gamma/\eta\xi$ in the overdamped regime. Both estimates are around 10^9 Hz for typical experiments.

6 Dynamical wetting regimes

In this concluding section we propose an organization of the different regimes of contact line motion.

6.1 Hydrodynamic versus thermally activated regime

The motion of contact lines can be deduced from a balance between power generated by capillary forces and the total energy dissipation taking place at different scales. There is substantial direct evidence that, beyond the threshold of contact angle hysteresis, the motion is dominated by viscous dissipation: (i) the predicted logarithmic variation of the interface slope with distance to the contact line is observed over one decade (Fig. 4a); (ii) the phenomenology of dynamical wetting transitions can, and can only, be recovered using hydrodynamics (Fig. 4b); (iii) the radius of curvature at the back of a V-shaped drop is observed to vary exponentially with Ca over one decade (Fig. 5); (iv) at low Reynolds numbers, the hydrodynamics describes quantitatively all experimental results, within an uncertainty that is comparable to the hysteresis (Fig. 4, 5, 6). This implies that the dominant dissipation is spread over 6 decades of length scales (from a nanometer to macroscopic distances to the contact line), and that molecular processes essentially appears as a cut-off to the dissipation. The tests cited above are much more delicate than the more classical measurement of θ_{ap} versus speed: the dynamic contact angle can usually be fitted accurately by various models (Le Grand et al. 2005, Seveno et al. 2009).

At low capillary numbers, close to the threshold of depinning, molecular scale processes generically become dominant due to surface heterogeneities. Indeed, even for the best physico-chemical coating ever realised (thiol brush), the hys-

teresis is still around 1% so that the Boltzmann factor appearing in Equation 18 is always much larger than unity. In this limit the contact line motion occurs by thermal activation (Fig. 7a). It is accurately described by Molecular Kinetic Theory, provided that the ratio of jump size and thermal length ξ/ℓ_T is much larger than unity. There are two noticeable exceptions where ξ/ℓ_T could be order unity such that there is no hysteresis: molecular dynamics simulations and liquid lenses.

The cross-over between these the thermally activated regime and the hydrodynamic regime takes place around the depinning transition ($\cos \theta \simeq \cos \theta_e \pm H$) where the energy barriers vanish. Figure 7b shows experimental measurements of apparent contact angles in the hydrodynamic regime. This figure obviously displays the hysteretic gap in θ_{ap} at very small Ca, which is the range where contact line motion is thermally activated. For future work, it will be interesting to observe thermally activated contact line motion and the hydrodynamic regime in a single experimental setup – comparing the data in Figs. 7a and b, the cross-over is expected between $\text{Ca} \sim 10^{-5}$ and 10^{-4} .

6.2 Inertial effects

Another transition takes place when inertial effects become comparable with viscosity. Figure 8 shows an extreme situation – the initial phase of the spreading of a water drop – which is totally controlled by inertia (Biance et al. 2004, Bird et al. 2008, Winkels et al. 2012). Also, the splashing in Fig. 1 will clearly involve inertial effects. To address the cross-over between viscous and inertial regimes, one can add perturbatively the inertial effect to the lubrication equation, which can be interpreted as a depth-averaged (Saint-Venant) equation. This method

was previously used in the context of Landau-Levich films (Koulago et al. 1995) and shows that inertia provides additional dissipation. Another approach using a perturbation expansion was followed by Cox (1998), which was qualitatively (not quantitatively) confirmed experimentally (Stoev et al. 1999). It remains to be investigated whether the effect of inertia could explain the differences when comparing low viscosity fluids like water to silicon oils (Podgorski et al. 2001, Winkels et al. 2011).

6.3 Future issues

1. The systematic procedure to capture the hydrodynamic and thermally activated regimes in a single description is to solve fluctuating hydrodynamics (Flekkoy & Rothman 1996). Is this feasible in the context of moving contact lines?
2. The activated contact line motion involves an activation length ξ of about 10 nm. What determines the activation surface ξ^2 ? How is it correlated with the surface roughness and/or with collective effects (Le Doussal et al. 2009)?
3. New challenges for moving contact lines emerge from the influence of additional mechanisms, such as the inclusion of liquid inertia.
4. Strong evaporation can affect the contact line motion. In particular if the liquid contains a solute such as polymers or colloids, this leads to stick-slip and patterning (Fig. 2).
5. Another type of complexity is related to the substrates. Contact line motion can be greatly influenced e.g. by patterns on superhydrophobic surfaces (Roach et al. 2008).

6. If the substrate is a soft solid that can be deformed by capillarity, dissipation can be dominated by the visco-elastic behaviour *of the solid* (Carre et al. 1996). How is the contact line motion influenced if the substrate is swelling, such as a gel or elastomer?

References

1. Andrew MK, Harris PD. 1995. Damping and gas viscosity measurements using a microstructure. *Sensors and Actuators A* 49:103–108
2. Ben Amar M, Cummings LJ, Pomeau Y. 2003. Transition of a moving contact line from smooth to angular. *Phys. Fluids* 15:2949–2960
3. Benkreira H, Ikin JB. 2010. Dynamic wetting and gas viscosity effects. *Chem. Eng. Sci.* 65:1790–1796
4. Benkreira H, Khan MI. 2008. Air entrainment in dip coating under reduced air pressures. *Chem. Eng. Sci.* 63:448–459
5. Berteloot G, Pham CT, Daerr A, Lequeux F, Limat L. 2008. Evaporation-induced flow near a contact line: Consequences on coating and contact angle. *Europhys. Lett.* 83
6. Biance AL, Clanet C, Quéré D. 2004. First steps of the spreading of a liquid droplet. *Phys. Rev. E* 69:016301
7. Bird JC, Mandre S, Stone HA. 2008. Short-time dynamics of partial wetting. *Phys. Rev. Lett.* 100
8. Blake TD. 2006. The physics of moving wetting lines. *J. Colloid Inter. Sci.* 299:1–13

9. Blake TD, De Coninck J. 2011. Dynamics of wetting and Kramers' theory. *Eur. Phys. J. Special Topics* 197:249–264
10. Blake TD, Haynes JM. 1969. Kinetics of liquid/liquid displacement. *J. Colloid Interface Sci.* 30:421–423
11. Blake TD, Ruschak KJ. 1979. A maximum speed of wetting. *Nature* 282:489–491
12. Bocquet L. 1993. Slipping of a fluid on a surface of controlled roughness. *C. R. Acad. Sc. Paris Série II* 316:7–12
13. Bocquet L, Charlaix E. 2010. Nanofluidics, from bulk to interfaces. *Chem. Soc. Rev.* 39:1073–1095
14. Bonn D, Eggers J, Indekeu J, Meunier J, Rolley E. 2009. Wetting and spreading. *Rev. Mod. Phys.* 81:739
15. Brochard-Wyart F, di Meglio JM, Quéré D. 1987. Dewetting - growth of dry regions from a film covering a flat solid or a fiber. *C. R. Acad. Sc. Paris Série II* 304:553–558
16. Buckingham R, Shearer M, Bertozzi A. 2003. Thin film traveling waves and the Navier slip condition. *SIAM J. Appl. Math.* 63:722–744
17. Burley R, Kennedy BS. 1978. Dynamic wetting and air entrainment at a liquid-solid-gas junction. In *Wetting, Spreading and Adhesion*, ed. JF Padday. Academic Press, London
18. Carlson A, Do-Quang M, Amberg G. 2009. Modeling of dynamic wetting far from equilibrium. *Phys. Fluids* 21
19. Carre A, Gastel J, Shanahan M. 1996. Viscoelastic effects in the spreading of liquids. *Nature* 379:432–434

20. Cazabat AM, Guena G. 2010. Evaporation of macroscopic sessile droplets. *Soft Matter* 6:2591–2612
21. Chan TS, Gueudre T, Snoeijer JH. 2011. Maximum speed of dewetting on a fiber. *Phys. Fluids* 23
22. Chan TS, Snoeijer JH, Eggers J. 2012. Theory of the forced wetting transition. *Submitted to Phys. Fluids*
23. Colinet P, Rednikov A. 2011. On integrable singularities and apparent contact angles within a classical paradigm Partial and complete wetting regimes with or without phase change. *Eur. Phys. J. Special Topics* 197:89–113
24. Cox RG. 1986. The dynamics of the spreading of liquids on a solid surface. part 1. viscous flow. *J. Fluid Mech.* 168:169–194
25. Cox RG. 1998. Inertial and viscous effects on dynamic contact angles. *J. Fluid Mech.* 357:249–278
26. Craster RV, Matar OK. 2009. Dynamics and stability of thin liquid films. *Rev. Mod. Phys.* 81:1131–1198
27. de Feijter JA. 1988. Thermodynamics of thin liquid films. In *Thin liquid films*, ed. IB Ivanov. Marcel Dekker, New York, 1–47
28. de Gennes PG. 1985. Wetting: statics and dynamics. *Rev. Mod. Phys.* 57:827–863
29. de Gennes PG. 1986. Transformation process for a horizontal soap film. *C. R. Acad. Sc. Paris Série II* 303:1275–1277
30. de Gennes PG, Brochart-Wyart F, D. Q. 2002. *Gouttes, bulles, perles et ondes*. Belin
31. de Gennes PG, Hua X, Levinson P. 1990. Dynamics of wetting: local contact angles. *J. Fluid Mech.* 212:55–63

32. De Ruiter J, Oh JM, van den Ende D, Mugele F. 2012. Dynamics of collapse of air films in drop impact. *Phys. Rev. Lett.* 108
33. Deegan RD, Bakajin O, Dupont TF, Huber G, Nagel SR, Witten TA. 1997. Capillary flow as the cause of ring stains from dried liquid drops. *Nature* 389:827–829
34. Delon G, Fermigier M, Snoeijer JH, Andreotti B. 2008. Relaxation of a dewetting contact line part 2: Experiments. *J. Fluid Mech.* 604:55
35. Deryaguin BV. 1943. On the thickness of a layer of liquid remaining on the walls of vessels after their emptying, and the theory of the application of photoemulsion after coating on the cine film. *Acta physico-chimica USSR* 20:349
36. Deryaguin BV, Levi SM. 1964. *Film Coating Theory*. Focal, London
37. Do-Quang M, Amberg G. 2009. The splash of a solid sphere impacting on a liquid surface: Numerical simulation of the influence of wetting. *Phys. Fluids* 21
38. Duez C, Ybert C, Clanet C, Bocquet L. 2007. Making a splash with water repellency. *Nat. Phys.* 3:180
39. Duffy BR, Wilson SK. 1997. A third-order differential equation arising in thin-film flows and relevant to tanner’s law. *Appl. Math. Lett.* 10:63
40. Eggers J. 2004. Hydrodynamic theory of forced dewetting. *Phys. Rev. Lett.* 93:094502
41. Eggers J. 2005. Existence of receding and advancing contact lines. *Phys. Fluids* 17:082106
42. Flekkoy E, Rothman D. 1996. Fluctuating hydrodynamic interfaces: Theory and simulation. *Phys. Rev. E* 53:1622–1643

43. Flitton JC, King JR. 2004. Surface-tension-driven dewetting of newtonian and power-law fluids. *J. Engin. Math.* 50:241–266
44. Getta T, Dietrich S. 1998. Line tension between fluid phases and a substrate. *Phys. Rev. E* 57:655
45. Golestanian R, Raphaël E. 2001. Dissipation in the dynamics of a moving contact line. *Phys. Rev. E* 64:031601–1–7
46. Hanggi P, Talkner P, Borkovec M. 1990. Reaction-rate theory - 50 years after Kramers. *Rev. Mod. Phys.* 62:251–341
47. Hocking LM. 1983. The spreading of a thin drop by gravity and capillarity. *Q. J. Mech. Appl. Math.* 36:55–69
48. Huang DM, Sendner C, Horinek D, Netz RR, Bocquet L. 2008. Water Slippage versus Contact Angle: A Quasiuniversal Relationship. *Phys. Rev. Lett.* 101
49. Huh C, Scriven LE. 1971. Hydrodynamic model of steady movement of a solid/liquid/fluid contact line. *J. Coll. Int. Sci.* 35:85–101
50. Jacqmin D. 2000. Contact-line dynamics of a diffuse fluid interface. *J. Fluid Mech.* 402:57–88
51. Kavehpour HP, Ovryn B, McKinley GH. 2003. Microscopic and macroscopic structure of the precursor layer in spreading viscous drops. *Phys. Rev. Lett.* 91:196104
52. Kirkwood J, Buff F. 1949. The statistical mechanical theory of surface tension. *Jou. Chem. Phys.* 17:338–343
53. Koulago A, Shkadov V, Quéré D, Deryck A. 1995. Film entrained by a fiber quickly drawn out of a liquid bath. *Phys. Fluids* 7:1221–1224

54. Kramers H. 1940. Brownian motion in a field of force and the diffusion model of chemical reactions. *Physica* 7:284–304
55. Landau LD, Levich BV. 1942. Dragging of a liquid by a moving plate. *Acta physico-chimica USSR* 17:42
56. Landau LD, Lifshitz EM. 1984. *Fluid Mechanics*. Pergamon: Oxford
57. Le Doussal P, Wiese KJ, Moulinet S, Rolley E. 2009. Height fluctuations of a contact line: A direct measurement of the renormalized disorder correlator. *Europhys. Lett.* 87
58. Le Grand N, Daerr A, Limat L. 2005. Shape and motion of drops sliding down an inclined plane. *J. Fluid Mech.* 541:293–315
59. Ledesma-Aguilar R, Nistal R, Hernández-Machado A, Pagonabarraga I. 2011. Controlled drop emission by wetting properties in driven liquid filaments. *Nature Materials* 10:367–371
60. Limat L, Stone HA. 2004. Three-dimensional lubrication model of a contact line corner singularity. *Europhys. Lett.* 65:365
61. Maleki M, Reyssat E, Quéré D, Golestanian R. 2007. On the landau-levich transition. *Langmuir* 23:10116
62. Mandre S, Mani M, Brenner MP. 2009. Precursors to splashing of liquid droplets on a solid surface. *Phys. Rev. Lett.* 102:134502
63. Marchand A, Chan TS, Snoeijer JH, Andreotti B. 2012. Air Entrainment by Viscous Contact Lines. *Phys. Rev. Lett.* 11
64. Maxwell J. 1878. On Stresses in Rarified Gases Arising from Inequalities of Temperature. *Phil. Trans. R. Soc. Lond.* 170:231–256
65. Merchant G, Keller J. 1992. Contact angles. *Phys. Fluids A* 4:477–485

66. Moffat JR, Sefiane K, Shanahan MER. 2009. Effect of tio₂ nanoparticles on contact line stick-slip behavior of volatile drops. *The Journal of Physical Chemistry B* 113:8860–8866
67. Monnery W, Svrcek W, Mehrotra A. 1995. Viscosity - a critical-review of practical predictive and correlative methods. *Can. J. Chem. Eng.* 73:3–40
68. Morris D, Hannon L, Garcia A. 1992. Slip length in a dilute gas. *Phys. Rev. A* 46:5279–5281
69. Mugele F, Baret JC. 2005. Electrowetting: from basics to applications. *J. Phys.: Condens. Matter* 17:R705
70. Nikolayev V, Beysens D. 2003. Equation of motion of the triple contact line along an inhomogeneous surface. *Europhys. Lett.* 64:763–768
71. Oron A, Davis SH, Bankoff SG. 1997. Long-scale evolution of thin liquid films. *Rev. Mod. Phys.* 69:931–980
72. Peters I, Snoeijer JH, Daerr A, Limat L. 2009. Coexistence of Two Singularities in Dewetting Flows: Regularizing the Corner Tip. *Phys. Rev. Lett.* 103
73. Pismen LM. 2001. Nonlocal diffuse interface theory of thin films and moving contact line. *Phys. Rev. E* 64:021603
74. Pismen LM, Pomeau Y. 2000. Disjoining potential and spreading of thin layers in the diffuse interface model coupled to hydrodynamics. *Phys. Rev. E* 62:2480–2492
75. Podgorski T, Flesselles JM, Limat L. 2001. Corners, cusps, and pearls in running drops. *Phys. Rev. Lett.* 87:036102(1)–(4)
76. Prevost A, Rolley E, Guthmann C. 1999. Thermally activated motion of the

- contact line of a liquid helium-4 meniscus on a cesium substrate. *Phys. Rev. Lett.* 83:348–351
77. Qian T, Wang XP, Sheng P. 2004. Power-law slip profile of the moving contact line in two-phase immiscible flows. *Phys. Rev. Lett.* 93:094501
78. Qian T, Wang XP, Sheng P. 2006. A variational approach to moving contact line hydrodynamics. *J. Fluid Mech.* 564:333–360
79. Quéré D. 1991. On the minimal velocity of forced spreading in partial wetting (in french). *C. R. Acad. Sci. Paris, Serie II* 313:313–318
80. Rame E, Garoff S. 1996. Microscopic and macroscopic dynamic interface shapes and the interpretation of dynamic contact angles. *J. Colloid Interface Sci.* 177:234–244
81. Redon C, Brochard-Wyart F, Rondelez F. 1991. Dynamics of dewetting. *Phys. Rev. Lett.* 66:715
82. Reiter G. 1992. Dewetting of thin polymer films. *Phys. Rev. Lett.* 68:75
83. Ren W, E W. 2007. Boundary conditions for the moving contact line problem. *Phys. Fluids* 19:022101
84. Rio E, Daerr A, Andreotti B, Limat L. 2005. Boundary conditions in the vicinity of a dynamic contact line: Experimental investigation of viscous drops sliding down an inclined plane. *Phys. Rev. Lett.* 94:024503
85. Roach P, Shirtcliffe NJ, Newton MI. 2008. Progress in superhydrophobic surface development. *Soft Matter* 4:224–240
86. Rolley E, Guthmann C. 2007. Dynamics and hysteresis of the contact line between liquid hydrogen and cesium substrates. *Phys. Rev. Lett.* 98:166105

87. Rowlinson JS, Widom B. 1982. *Molecular Theory of Capillarity*. Oxford: Clarendon
88. Saulnier F, Raphaël E, de Gennes PG. 2002. Dewetting of thin polymer films near the glass transition. *Phys. Rev. Lett.* 88:196101
89. Schwartz LW, Roux D, Cooper-White JJ. 2005. On the shapes of droplets that are sliding on a vertical wall. *Physica D* 209:236
90. Sedev RV, Petrov JG. 1991. The critical condition for transition from steady wetting to film entrainment. *Colloids and Surfaces* 53:147
91. Seemann R, Herminghaus S, Jacobs K. 2001. Dewetting patterns and molecular forces: A reconciliation. *Phys. Rev. Lett.* 86:5534–5537
92. Seveno D, Vaillant A, Rioboo R, Adao H, Conti J, De Coninck J. 2009. Dynamics of Wetting Revisited. *Langmuir* 25:13034–13044
93. Simpkins PG, Kuck VJ. 2000. Air entrapment in coatings by way of a tip-streaming meniscus. *Nature* 403:641–643
94. Snoeijer J, Le Grand N, Limat L, Stone HA, Eggers J. 2007a. Cornered drop and rivulets. *Phys. Fluids* 19:042104
95. Snoeijer JH. 2006. Free surface flows with large slopes: beyond lubrication theory. *Phys. Fluids* 18:021701
96. Snoeijer JH, Andreotti B. 2008. A microscopic view on contact angle selection. *Phys. Fluids* 20
97. Snoeijer JH, Andreotti B, Delon G, Fermigier M. 2007b. Relaxation of a dewetting contact line part 1: A full-scale hydrodynamic calculation. *J. Fluid Mech.* 579:63

98. Snoeijer JH, Delon G, Fermigier M, Andreotti B. 2006. Avoided critical behavior in dynamically forced wetting. *Phys. Rev. Lett.* 96:174504
99. Snoeijer JH, Eggers J. 2010. Asymptotics of the dewetting rim. *Phys. Rev. E* 82:056314
100. Stoev K, Ramé E, Garoff S. 1999. Effects of inertia on the hydrodynamics near moving contact lines. *Phys. Fluids* 11:3209
101. Thiele U. 2003. Open questions and promising new fields in dewetting. *Eur. Phys. J. E* 12:409
102. Thiele U, Neuffer K, Bestehorn M, Pomeau Y, Velarde MG. 2002. Sliding drops on an inclined plane. *Colloid Surf. A* 206:87–104
103. Tsai P, van der Veen RCA, van de Raa M, Lohse D. 2010. How micropatterns and air pressure affect splashing on surfaces. *Langmuir* 26:16090
104. Voinov OV. 1976. Hydrodynamics of wetting [english translation]. *Fluid Dynamics* 11:714–721
105. Watanabe S, Inukai K, Mizuta S, Miyahara MT. 2009. Mechanism for Stripe Pattern Formation on Hydrophilic Surfaces by Using Convective Self-Assembly. *Langmuir* 25:7287–7295
106. Winkels K, Weijs JH, Eddi A, Snoeijer JH. 2012. Universal spreading dynamics of liquid drops on partially wetting surfaces. *Phys. Rev. Lett.* 11
107. Winkels KG, Peters IR, Evangelista F, Riepen M, Daerr A, et al. 2011. Receding contact lines: From sliding drops to immersion lithography. *Eur. Phys. J. Special Topics* 192:195
108. Xu L, Zhang WW, Nagel SR. 2005. Drop splashing on a dry smooth surface. *Phys. Rev. Lett.* 94:184505

109. Yue P, Feng JJ. 2011. Can diffuse-interface models quantitatively describe moving contact lines? *Eur. Phys. J. Special Topics* 197:37–46

7 Key Terms

- Laplace pressure: difference in pressure $\Delta p = \gamma\kappa$ across an interface of curvature κ , induced by capillary forces.
- Capillary length: length scale arising from the balance of surface tension and gravity, determining the rise of a static meniscus.
- Multi-scale: indicates that physical processes at very different length scales are intimately coupled and cannot be separated.
- Thermal activation: motion towards a lower energy state across an energy barrier, induced by a rare thermal fluctuation.
- Lubrication approximation: systematic method to simplify the hydrodynamic equations, which is valid for a quasi parallel flow (for small contact angles).
- Matching: term borrowed from “matched asymptotic expansion”. It is often loosely used to indicate the coupling of solutions at different scales.
- Dip-coating: common geometry to study wetting and coating, where a solid surface is plunged into or withdrawn from a bath.
- Contact angle hysteresis: even the cleanest substrates allow for a finite range of static contact angles, rather than a single equilibrium contact angle.
- Apparent contact angle: this is not the true angle of the interface, but an extrapolated angle based on the large scale meniscus profile.

- Viscous bending: viscosity-induced curvature of the interface, with a local contact angle that varies logarithmically with the distance to the contact line.

8 Sidebar, to be placed after Section 2.2: Evaporation

A similar corner singularity is encountered when liquid drops evaporate on a surface (Fig. 2) (Deegan et al. 1997). For small contact angles, the evaporative flux diverges as $j = J_0/\sqrt{x}$, where x is the distance to the contact line and J_0 is a constant. Inside the liquid, this induces a flow $U_{\text{evap}} \sim J_0/\theta\sqrt{x}$, oriented towards the contact line. Interestingly, an evaporative contact line usually recedes over the substrate, in the direction opposite to U_{evap} (Cazabat & Guena 2010). Comparing the receding velocity U with U_{evap} , one obtains a length scale $\ell_{\text{evap}} = (J_0/\theta U)^2$ that can be as large as 100 microns (Berteloot et al. 2008). This length separates regions where mass transport is towards or directed away from the contact line (Fig. 2a). When the liquid contains colloidal particles or polymers, the evaporation leads to self-assembly and pattern formation. A well known example is provided by the dark edge of a coffee stain, consisting of particles transported by U_{evap} . Figure 2c shows a case where this has induced a stick-slip motion of the contact line, leaving various deposits.

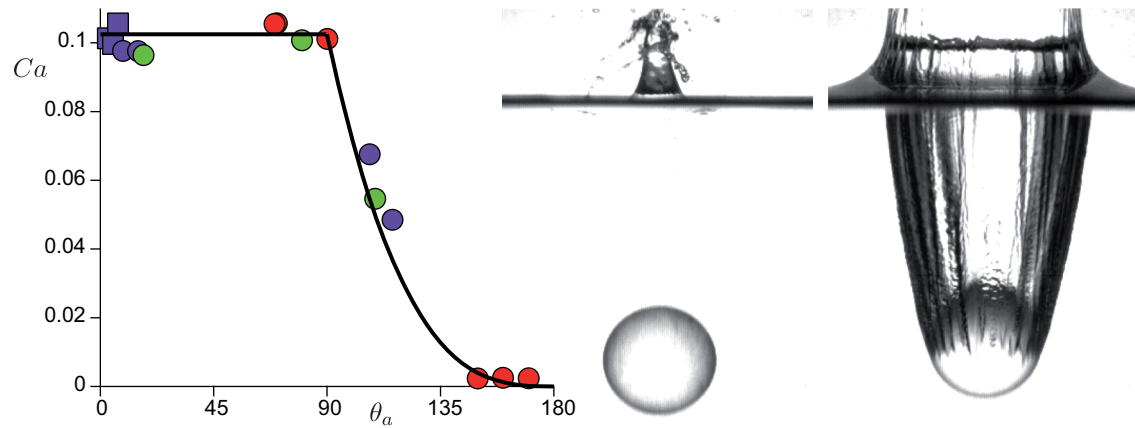


Figure 1: Impact of two spheres differing only in wettability via a nanometric coating on their surface. Left: hydrophilic, $\theta_e = 15^\circ$. Right: hydrophobic $\theta_e = 100^\circ$. Threshold capillary number Ca for air entrainment as a function of the advancing contact angle θ_a of the impacting body. Data correspond to various sphere diameters (differing by color) and various viscosities (differing by symbol). After Duez et al. (2007)

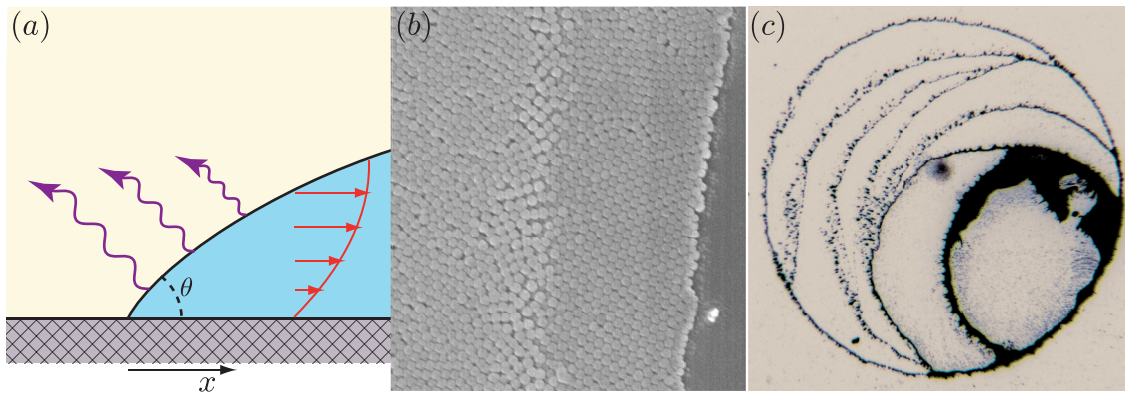


Figure 2: (a) The evaporative flux for a drop of volatile liquid is strongest near the contact line (Deegan et al. 1997). The mass transport inside the drop arises from a competition between the evaporative flux (inducing mass flux to the left) and the receding velocity of the contact line (inducing mass flux to the right). After Berteloot et al. (2008). (b) Magnified image of a stripe pattern left by the moving contact line of a dilute suspension of silica spheres (diameter 123 nm). A multi-layer close-packed array of particles can be observed. After Watanabe et al. (2009). (c) Photograph of solid surface after evaporation of dilute suspension of TiO_2 nanoparticles in ethanol. Rings of accumulated particles correspond to the "sticking phase of a stick-slip cycle. After Moffat et al. (2009).

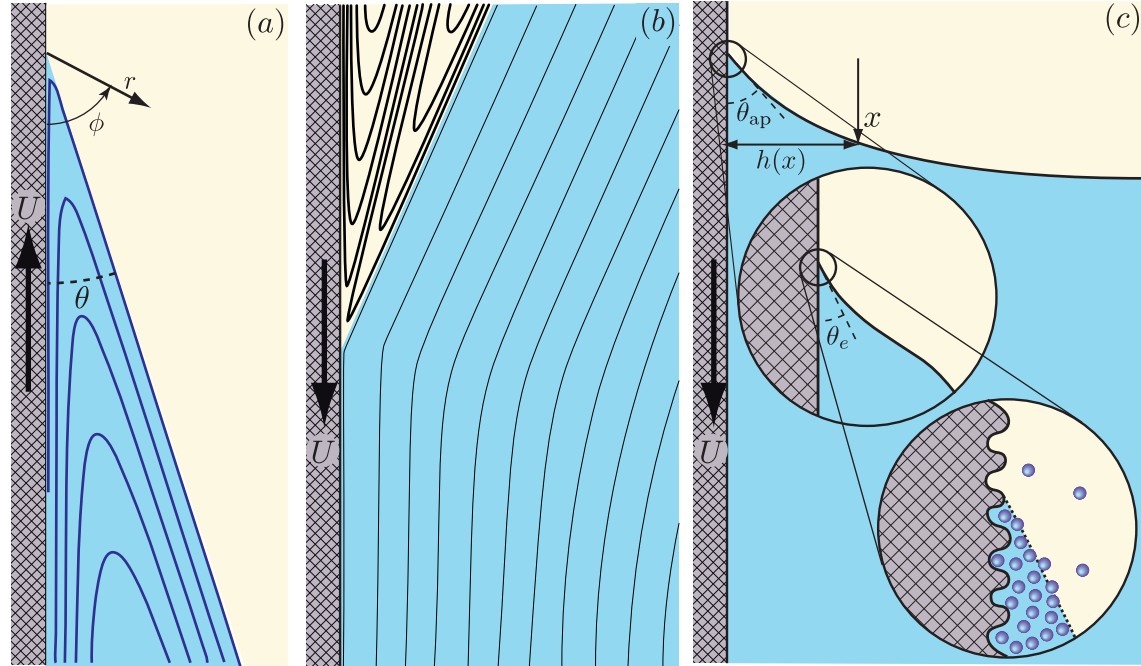


Figure 3: Streamlines in a perfect wedge (Huh & Scriven 1971) of angle θ for (a) a receding contact line (one phase flow, θ close to 0), and for (b) an advancing contact line (two phase flow, with θ close to π). In the advancing case, the viscous dissipation in the gas phase can dominate over the liquid phase due to the strongly confined circulation in the gas wedge. (c) Interface profile $h(x)$ for a plunging plate under partial wetting conditions. The interface near the contact line is highly curved so that the apparent contact angle θ_{ap} on the macroscopic scale is much larger than the true contact angle θ_e as nanoscopic scale. The intermediate zoom represents the hydrodynamic regime that is governed by viscosity and surface tension. After Bonn et al. (2009).

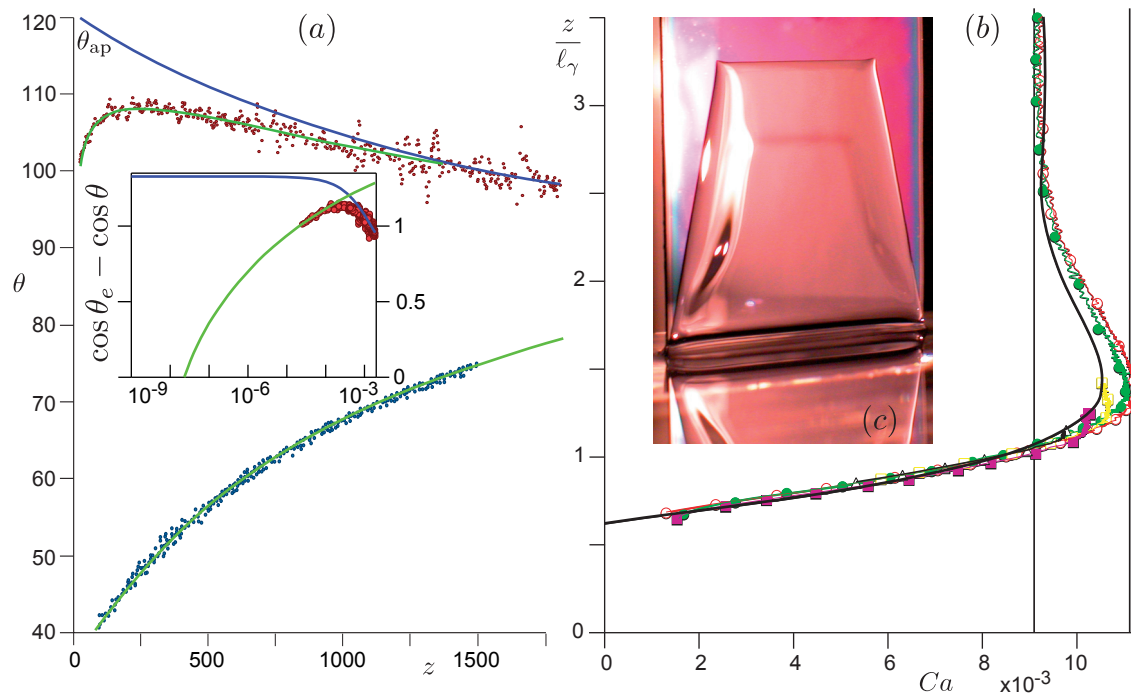


Figure 4: (a) Shape of a dynamic interface measured by Rame & Garoff (1996) for a coated cylinder plunging in a bath of silicon oil ($\theta_e \sim 35^\circ$). The dots represent the local angle of the meniscus with respect to the substrate, θ , as a function of the horizontal distance to the contact line. Blue dots: static meniscus $Ca = 0$. Red dots: dynamical meniscus $Ca = 0.1$. The inset of the figure shows the same data on a logarithmic scale. The green solid line is the hydrodynamic prediction in the visco-capillary regime. Experimental points do not reach below distances of about 10 microns from the contact line, but the interface is curved down to nanometer scales. The blue line is the fit of the macroscopic shape of the interface ($\theta \rightarrow 90^\circ$ at the bath) by the static solution. The extrapolation to 120° defines the apparent contact angle θ_{ap} . (b) A partially wetting plate is withdrawn from a silicon oil bath liquid at capillary number Ca , which forms a dynamic contact line at height $z(Ca)$. The solid line is derived from the multi-scale lubrication theory. The maximum capillary number is reached close to $z_c = \sqrt{2}\ell_\gamma$, which corresponds to $\theta_{ap} = 0$. After Delon et al. (2008). (c) A liquid film is entrained above the critical capillary number Ca_c . The film consists of two parts of incompatible

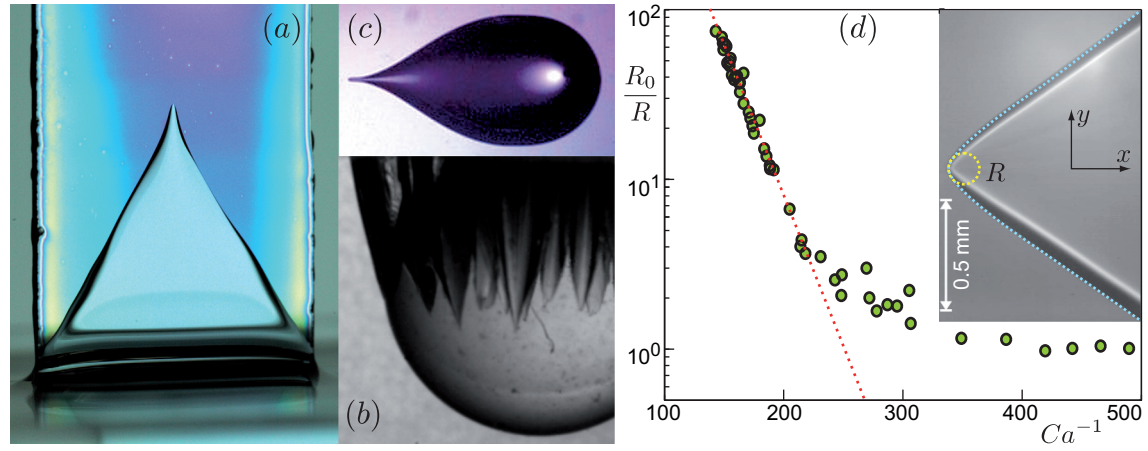


Figure 5: V-shapes appearing at the dynamical wetting transition. (a) Dip-coating (Delon et al. 2008). (b) Sphere plunging in a bath (Duez et al. 2007) (as in Fig. 1), (c) Silicon oil drop moving down an inclined plane (Podgorski et al. 2001). (d) Radius of curvature R of the rounded edge of a corner drop as a function of Ca . The dotted line is the prediction by hydrodynamic theory. After Peters et al. (2009).

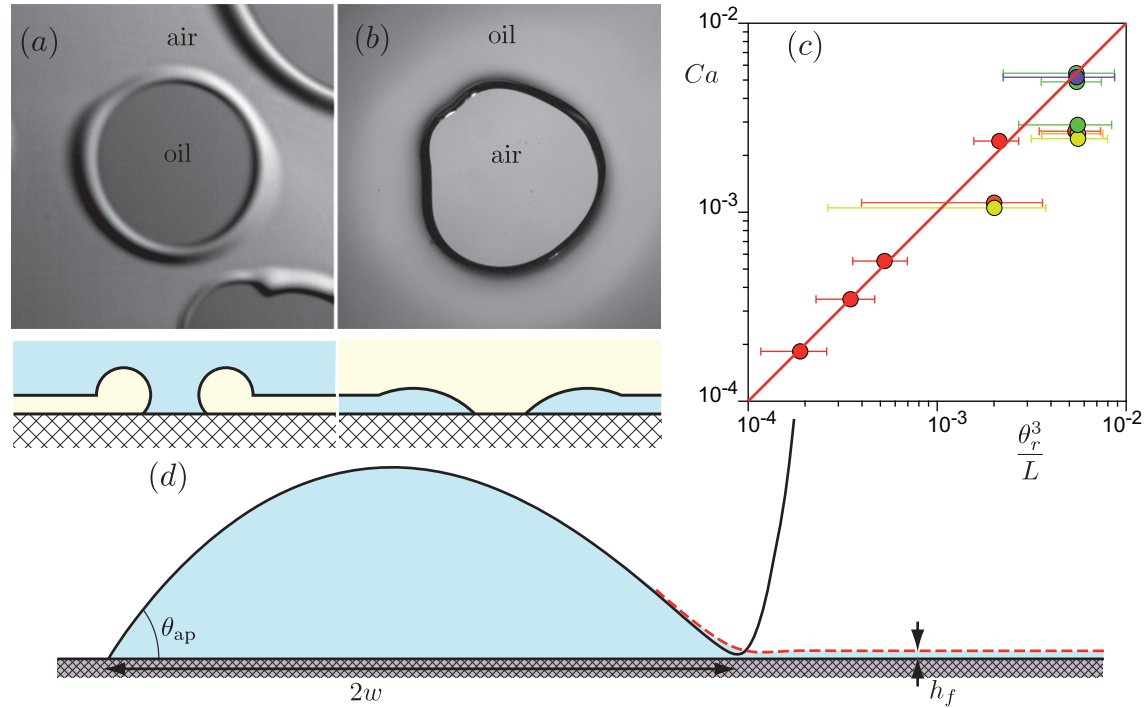


Figure 6: Dewetting holes. (a) Picture and schematic of a rewetting hole observed when a film of air is entrained dynamically into a silicon oil bath. (b) Picture and schematic of a dewetting hole observed for a film of silicon oil on a fluorinated substrate. (c) Dewetting capillary number as a function of the receding contact angle θ_r . L is the logarithmic factor appearing in Equation 9. Different colors represent different molecular weights of the liquid. The error bars mainly reflect the uncertainty on the contact angle. After Redon et al. (1991). (d) Cross-section of the solution obtained by asymptotic matching of the receding front (black solid line) and the advancing front (dashed red line). After Snoeijer & Eggers (2010).

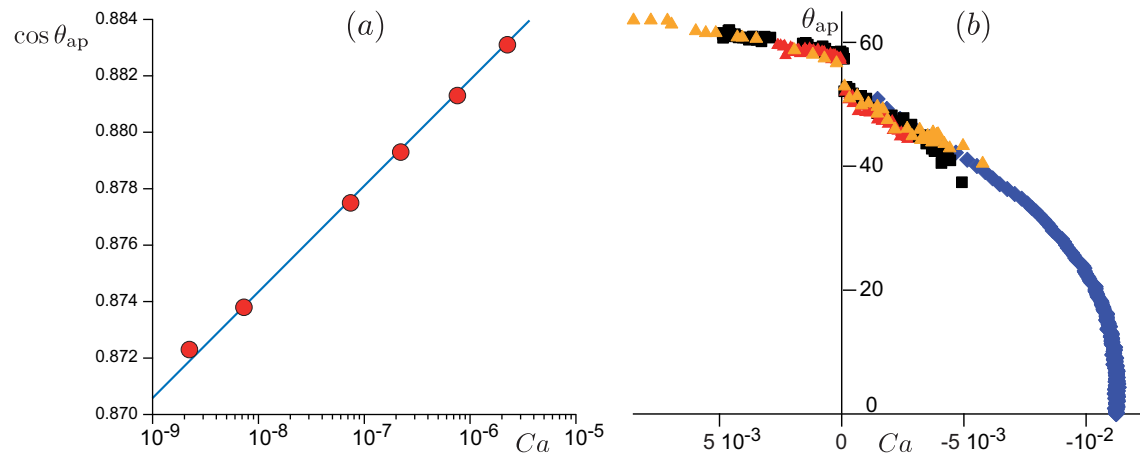


Figure 7: (a) Relation between the apparent contact angle θ_{ap} and the capillary number Ca in a dip-coating experiment performed with liquid hydrogen on a cesium substrate. The exponential dependence on velocity is the signature of a thermally activated regime below $Ca = 10^{-5}$. After Rolley & Guthmann (2007). (b) Same for silicon oil on a fluorinated substrate (blue symbols, Delon et al. (2008)) and for a drop of the same fluid flowing down an inclined plane (red, orange and black symbols, Rio et al. (2005)). This quantitative agreement with the multi-scale lubrication theory (Fig. 4b) points to a hydrodynamic regime above $Ca = 10^{-4}$.

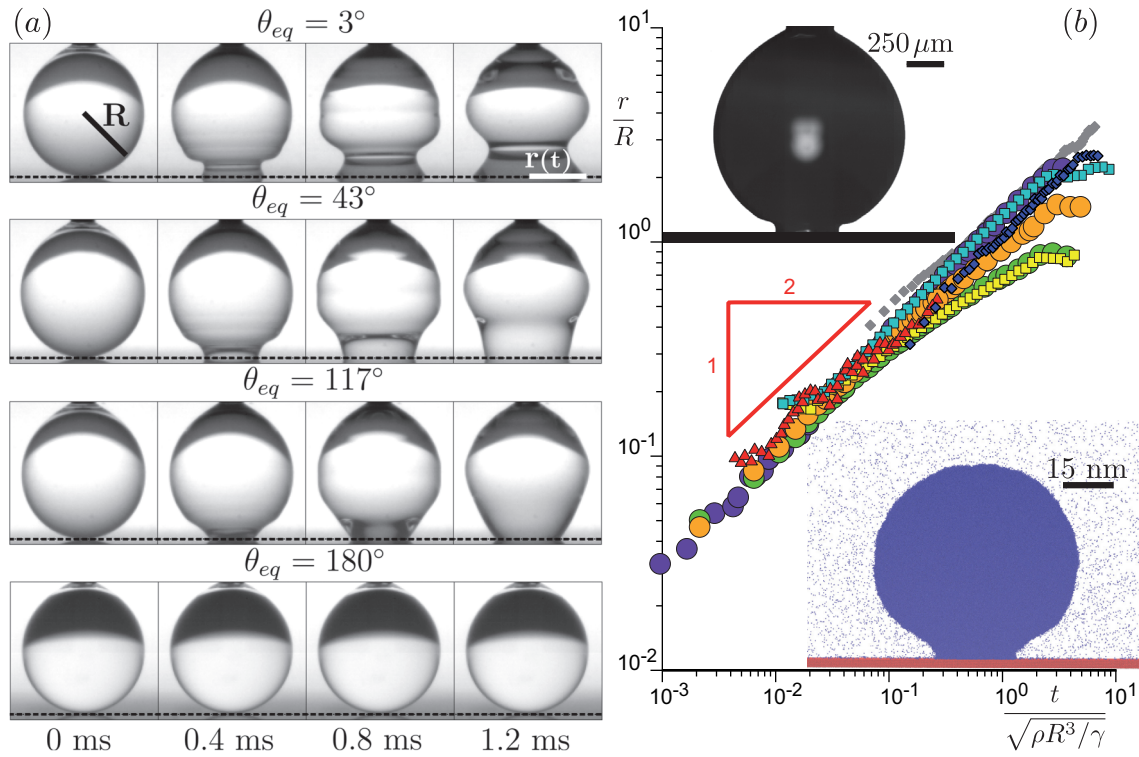


Figure 8: Inertial spreading of water drops of radius $R = 0.82$ mm on different surfaces. After Bird et al. (2008). (b) Contact radius r as a function of time t for different equilibrium contact angles. Data from Bianco et al. (2004), Bird et al. (2008), Winkels et al. (2012). The time is rescaled by the inertial time $\sqrt{\rho R^3 / \gamma}$ based on density ρ and surface tension. Insets: initial stages of drop spreading for a water drop and a simulated Lennard-Jones drop (Winkels et al. 2012).